

## **SIMULATION OF SHOCK WAVE LOADED CONCRETE WITH DISCRETE CRACKS**

**Martin Larcher<sup>1</sup>, Lothar Stempniewski<sup>1</sup>**

<sup>1</sup>Institut für Massivbau und Baustofftechnologie  
Universität Karlsruhe (TH), D-76128 Karlsruhe  
larcher@ifmb.uka.de, stempniewski@ifmb.uka.de

**Keywords:** Shock Wave, Discrete Cracks, Element-free Galerkin Method, Hugoniot, Strain Rate Effect, Blasting.

**Abstract.** *Aim of the presented research is to simulate the blasting of concrete. The element-free Galerkin method is used to describe discrete cracks in concrete. The cracks are developed using a simple St. Venant criterion. The nonlinear material behavior of concrete is described by a cohesive crack model. The usability of the combination of discrete cracks with the described material model is shown by comparison of static experimental results with numerical results. In consideration of the strain rate effect and the Hugoniot-curve shock waves in concrete are calculated. The simulation of the blasted concrete results in a realistic crack pattern.*

## 1 INTRODUCTION

Simulation of high dynamic loading of concrete needs special material models. The development of shock waves and consequently the discontinuity in front of the shock wave have to be considered. Another challenge is the calculation of the concrete cracking.

The idea of this research is the use of discrete cracks with a cohesive crack model instead of a damage material model. The results of these calculations will be compared with experimental results of blasted concrete.

## 2 ELEMENT-FREE GALERKIN METHOD

### 2.1 MLS-Interpolation

Belytschko [3] proposed the element-free Galerkin method (EFG) which approximates a field by using a moving least-squares interpolation (MLS interpolation). The following equation is used for the approximation of the displacement field

$$u^h(\mathbf{x}) = \sum_{i=1}^n \phi_i^k(\mathbf{x}) u_i = \mathbf{p}^T \cdot \mathbf{a} \quad (1)$$

The shape function  $\phi$  is built from monomial functions  $\mathbf{p}$ . A linear 2-dimensional example for  $\mathbf{p}$  is

$$\mathbf{p}(\mathbf{x}) = (1 \ x \ y)^T \quad (2)$$

The vector  $\mathbf{a}$  is calculated by the minimisation of the interpolation error  $J_i$

$$J_i(\mathbf{a}, \mathbf{x}) = \sum_{i=1}^n w_i(\mathbf{x}) \cdot (u_i - p_i^T(\mathbf{x}) \cdot \mathbf{a})^2 \quad (3)$$

By using the following matrices

$$\mathbf{A} = \mathbf{P}^T \mathbf{W}(\mathbf{x}) \mathbf{P} \quad (4)$$

$$\mathbf{B} = \mathbf{P}^T \mathbf{W}(\mathbf{x}) \quad (5)$$

with

$$\mathbf{P} = \begin{pmatrix} p_1(\mathbf{x}_1) & p_2(\mathbf{x}_1) & \dots & p_m(\mathbf{x}_1) \\ p_1(\mathbf{x}_2) & p_2(\mathbf{x}_2) & \dots & p_m(\mathbf{x}_2) \\ \vdots & \vdots & \ddots & \vdots \\ p_1(\mathbf{x}_n) & p_2(\mathbf{x}_n) & \dots & p_m(\mathbf{x}_n) \end{pmatrix} \quad (6)$$

and the weight matrix

$$\mathbf{W} = \begin{pmatrix} w(\mathbf{x} - \mathbf{x}_1) & 0 & \dots & 0 \\ 0 & w(\mathbf{x} - \mathbf{x}_2) & \dots & 0 \\ \vdots & \vdots & \ddots & \vdots \\ 0 & 0 & \dots & w(\mathbf{x} - \mathbf{x}_n) \end{pmatrix} \quad (7)$$

the derivation of the interpolation error becomes

$$\frac{\partial J_i(\mathbf{a}, \mathbf{x})}{\partial \mathbf{a}} = \mathbf{A}(\mathbf{x}) \cdot \mathbf{a} - \mathbf{B}(\mathbf{x}) \cdot \mathbf{u}_i = 0 \quad (8)$$

By solving equation( 8) for  $\mathbf{a}$ , the shape function can be written as

$$\phi = \mathbf{p}^T(\mathbf{x})\mathbf{A}^{-1}(\mathbf{x})\mathbf{B}(\mathbf{x}) \quad (9)$$

The weight function  $w$  depends on the distance  $\|\mathbf{x} - \mathbf{x}_i\|$ . The weight function can be written as

$$w(\mathbf{x}) = w(s) \text{ with } s = \frac{\|\mathbf{x} - \mathbf{x}_i\|}{h_i} \quad (10)$$

The size of the radius of influence is discussed in chapter 2.3.  $w(s)$  should be a monotone falling function with

$$\begin{aligned} w(s) &= 1 \text{ for } s = 0 \\ w(s) &> 0 \text{ for } s < 1 \\ w(s) &= 0 \text{ for } s \geq 1 \end{aligned} \quad (11)$$

A common spline function (shown in Figure 1) fulfills these requirements

$$w(s) = 1 - 6s^2 + 8s^3 - 3s^4 \quad (12)$$

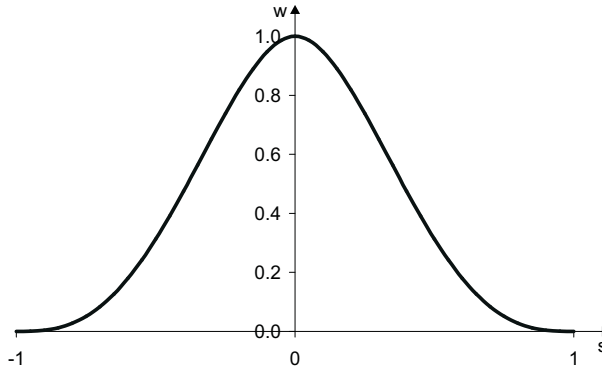


Figure 1: Spline function used as weight function

## 2.2 MLS-Interpolation and Cracks

Cracks can be implemented in EFG by cutting off the weight functions (and herewith the shape functions) at the location of the crack (Figure 2). The domain of the examined node is divided into two subdomains (Figure 3) – subdomain B beyond the crack and subdomain A on the side of the node. In subdomain A the spline function  $w$  is the same as before, in subdomain B it is set to

$$w(\mathbf{x}) = 0 \text{ for all } \mathbf{x} \in B. \quad (13)$$

It is sometimes difficult to differentiate which node is in the subdomain A and which node belongs to subdomain B. Ventura [12] uses a visibility check for the problem of locating the points (Figure 3). This method has one disadvantage – the shape functions become discontinuous. In some cases – especially in explicit time integrations – discontinuous shape functions are the reason that may lead to missing convergence.

Belytschko proposes a method to avoid this discontinuous shape functions by using the diffraction and the transparency method. Both methods generate continuous shape functions. The results of both methods differ from the result with the visibility method due to the different influence of the node near the crack tip.

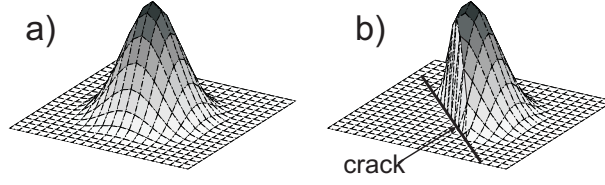


Figure 2: Weight function a) without crack b) with crack

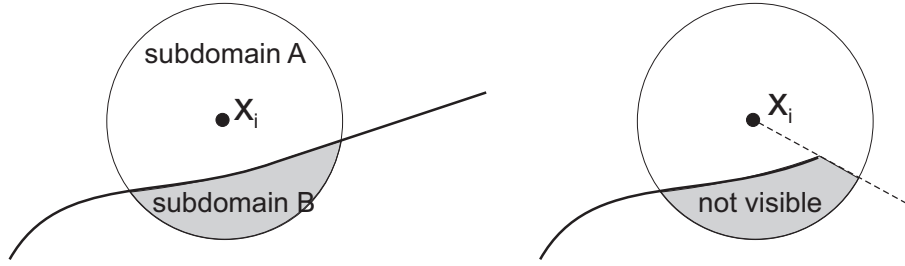


Figure 3: Visibility check

### 2.3 Domain of influence

Another problem is the choice of the radius of support  $h_i$ . If you choose  $h_i$  too small there are not enough nodes in the supported area and the approximation does not yield to a result. If the radius of support is too large, the difference between the equations at the nodes is so small that the stiffness matrix becomes singular.

In a regular mesh the number of nodes with influence within a supported area is smaller near cracks and boundaries. So it is reasonable to choose the radius of support by controlling the number of nodes in the supported area. The experience advises 4 to 10 nodes in a supported area.

### 2.4 Discretisation

The EFG method can be used to calculate different field functions. The discretisation of a displacement field by the EFG method is the following

$$\mathbf{u}(\mathbf{x}) = \mathbf{N}(\mathbf{x}) \cdot \mathbf{u}_i \quad (14)$$

with the matrix of the shape functions  $\mathbf{N}(\mathbf{x})$

$$\mathbf{N}(\mathbf{x}) = \begin{pmatrix} \varphi_i(\mathbf{x}) & 0 & \dots & \varphi_n(\mathbf{x}) & 0 \\ 0 & \varphi_i(\mathbf{x}) & \dots & 0 & \varphi_n(\mathbf{x}) \end{pmatrix} \quad (15)$$

The strains can be determined by

$$\boldsymbol{\epsilon}(\mathbf{x}) = D\mathbf{u}(\mathbf{x}) = D\mathbf{N}(\mathbf{x})\mathbf{u}_i(\mathbf{x}) = \mathbf{B}(\mathbf{x})\mathbf{u}_i(\mathbf{x}) \quad (16)$$

with the  $\mathbf{B}$ -Matrix

$$\mathbf{B}(\mathbf{x}) = \begin{pmatrix} \varphi_{i,x}(\mathbf{x}) & 0 & \dots & \varphi_{n,x}(\mathbf{x}) & 0 \\ 0 & \varphi_{i,y}(\mathbf{x}) & \dots & 0 & \varphi_{n,y}(\mathbf{x}) \\ \varphi_{i,y}(\mathbf{x}) & \varphi_{i,x}(\mathbf{x}) & \dots & \varphi_{n,y}(\mathbf{x}) & \varphi_{n,x}(\mathbf{x}) \end{pmatrix} \quad (17)$$

The equilibrium equation over all degrees of freedom is

$$\int_{\Omega} \mathbf{B}^T(\mathbf{x}) \cdot \boldsymbol{\sigma} d\Omega = \int_{\Omega} \mathbf{N}^T(\mathbf{x}) \cdot \mathbf{b} d\Omega + \int_{\Gamma_t} \mathbf{N}^T(\mathbf{x}) \cdot \bar{\mathbf{t}} d\Gamma \quad (18)$$

Equation 18 can be integrated by integration methods shown in chapter 2.5.

### 2.5 Integration – computing time

There are two possible ways to integrate over the domain: the integration with a background mesh and the nodal integration.

The integration with a background mesh is easy to implement because the integration is similar to the finite element method. There are three possibilities to place the nodes and the integration points:

- All nodes in the system are the corners of the integration cells.
- The nodes are the corners of the integration cells, but there are additional nodes.
- The nodes are not the corner of the integration cells.

The first case requires a regular mesh; the second and the third case do not require a regular mesh. Irregular meshes are interesting for calculating discontinuities. The mesh can be refined around the discontinuities and can yield to a better result.

Most investigations within this work use the explicit time integration. Due to the high number of nodes used with the explicit time integration an adaptation of the mesh is not necessary. Therefore the edges of the integration cells are used as nodes. The adaptation used in the static calculations (chapter 4.1) bases on a fine mesh kept constant from the beginning of the calculation.

Investigations have shown that the result is dependent on the discretisation and the number of integration points. Figure 4 shows a beam loaded by tension and bending. The analytical result for the bending loading is given by Timoschenko [11].

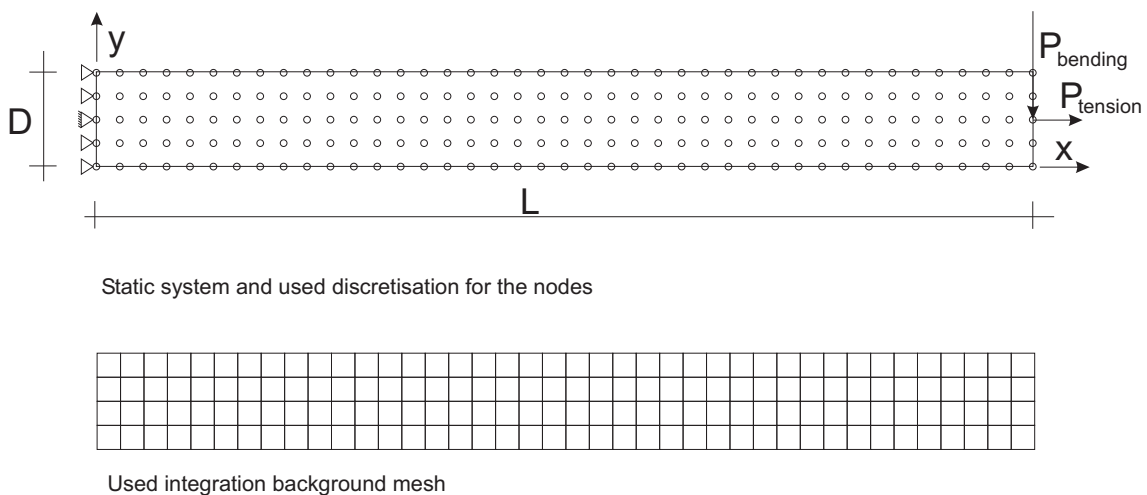


Figure 4: Used model of a beam

The relative error of the calculation results for the beam under tension loading does not show a dependence on the number of integration points (Figure 5). The relative error for the beam

under bending loading shows a small dependence on the number of integration points – but the error becomes smaller with a higher discretisation. As the deviations are very small and the discretisations are very large, two integration points are used in each direction.

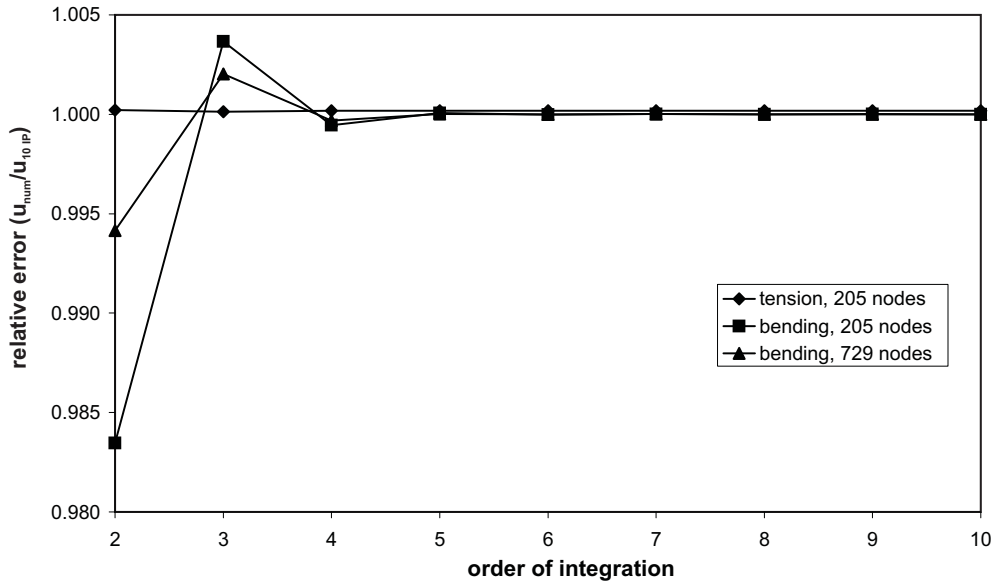


Figure 5: Relative error of several integration meshes related to a mesh with 10 integration points in each direction

The computing time for the calculation with the background integration is high. Quicker calculations are possible with the nodal integration proposed by Beissel [2]. This integration method calculates integration constants for each node. The method becomes more independent of the mesh but Hourglass modes are possible and therefore it is not useful in combination with the explicit time integration.

The differences in the computing time are shown in Figure 6. If EFG is used with explicit time integration the computing time is acceptable. So in the presented work the integration with a background mesh is used.

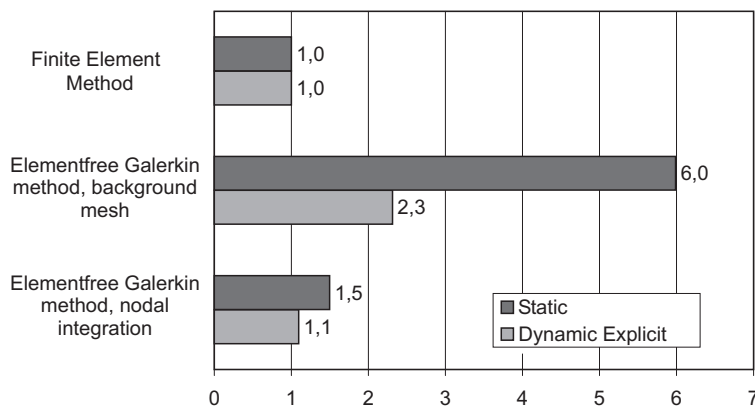


Figure 6: Computing time of various integration methods related to finite element method

### 3 MATERIAL MODEL

Two general material models for concrete can be distinguished: smeared and discrete crack models. In a smeared crack model the strains resulting from a crack are dispersed over one or more elements. In contrast to discrete cracks the location of the crack is not stored. A discrete crack model helps to consider the fragmentation of the concrete for example after high dynamic loading. In the presented work discrete cracks are implemented with EFG. The use of discrete cracks with a fracture process zone makes it possible to use a material model without damage formulation.

For high dynamic loading there are two effects to be considered for the calculation: the building of shock waves and the strain rate effect.

#### 3.1 Nonlinear stress-strain relation

Concrete responds to loading very nonlinear. A linear fracture mechanic is not usable. In this work cohesive cracks are implemented to describe the effects in the micro and meso scale cracking. In a zone – called fracture process zone (FPZ) – the stresses between the crack sides decreases from tensile strength to zero. The length of the FPZ can be calculated with the crack energy. For the distribution of the stresses between the crack sides an exponential or a bilinear function can be used. The exponential function has the form

$$\sigma_{ccs} = f_{t,dyn} \cdot \left(1 - \frac{w}{w_{max}}\right)^\alpha \quad (19)$$

with the dynamic strength  $f_{t,dyn}$  – in a static case the dynamic strength is replaced with the static strength. The critical crack opening  $w_{max}$  can be calculated using the fracture energy  $G_f$ .

$$G_f = \int_0^{w_{max}} \sigma_{ccs} dw = \frac{1}{1 + \alpha} f_{t,dyn} w_{max} \quad (20)$$

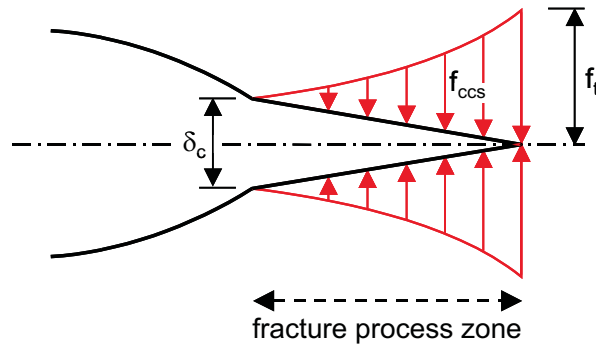


Figure 7: Fracture process zone

Akkermann [1] proposes a bilinear function

$$\begin{aligned} \sigma_{ccs} &= \frac{(\beta_t - 1) \cdot f_{ct}}{\alpha_t \cdot w_{max}} w + f_{ct} & \text{for } w < \alpha_t \cdot w_{max} \\ \sigma_{ccs} &= -\frac{\beta_t \cdot f_{ct}}{w_{max}(1 - \alpha_t)} w + \frac{\beta_t \cdot f_{ct}}{1 - \alpha_t} & \text{for } w > \alpha_t \cdot w_{max} \end{aligned} \quad (21)$$

Roelfstra [8] uses a value of 0.14 for the coefficient  $\alpha_t$ ; the coefficient  $\beta_t$  depends on the compression strength of concrete

$$\begin{aligned} \beta_t &= 0.25 && \text{for } f_c < 30 \text{ MPa} \\ \beta_t &= 0.25 - 0.0015 \cdot (f_c[\text{MPa}] - 30) && \text{for } f_c > 30 \text{ MPa} \end{aligned} \quad (22)$$

The maximal crack opening is calculated by integrating the stresses over the crack opening

$$w_{max} = \frac{2 \cdot G_f}{f_{ct}(\alpha_t + \beta_t)} \quad (23)$$

The differences in numerical results using both distributions of the stress are shown in Figure 8 and chapter 4.1.

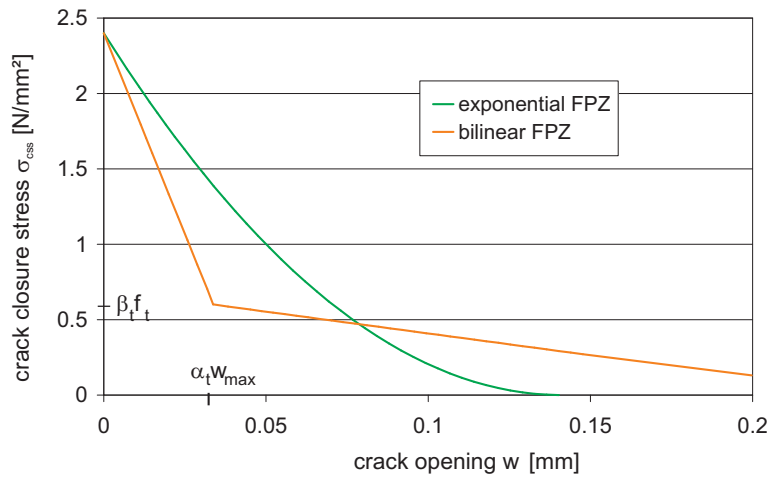


Figure 8: Fracture process zone

A St. Venant criterion is used to identify the growth of the crack. The direction of the crack growth is orthogonal to the direction of the principle strain.

### 3.2 Hugoniot

The nonlinear volumetric stress-strain relation (see Figure 9) is the cause for the development of shock waves. The first part of the volumetric strain-pressure curve is the elastic part. The gradient in this part is the elastic compression modulus. By increasing volumetric strains the micropores in the concrete are damaged. The gradient of the stress-strain relation becomes smaller than the compression modulus – the waves moves more slowly. After the destruction of the micropores the stiffness of the concrete is getting higher due to the compaction of the material (Hugoniot). The increased stiffness is the reason for the development of the shock waves.

In the presented work a Y-function is used to consider the increase of stiffness. The Young's modulus  $E$  has to be multiplied with this function.

$$E_{tot} = Y(\epsilon_v) \cdot E \quad (24)$$

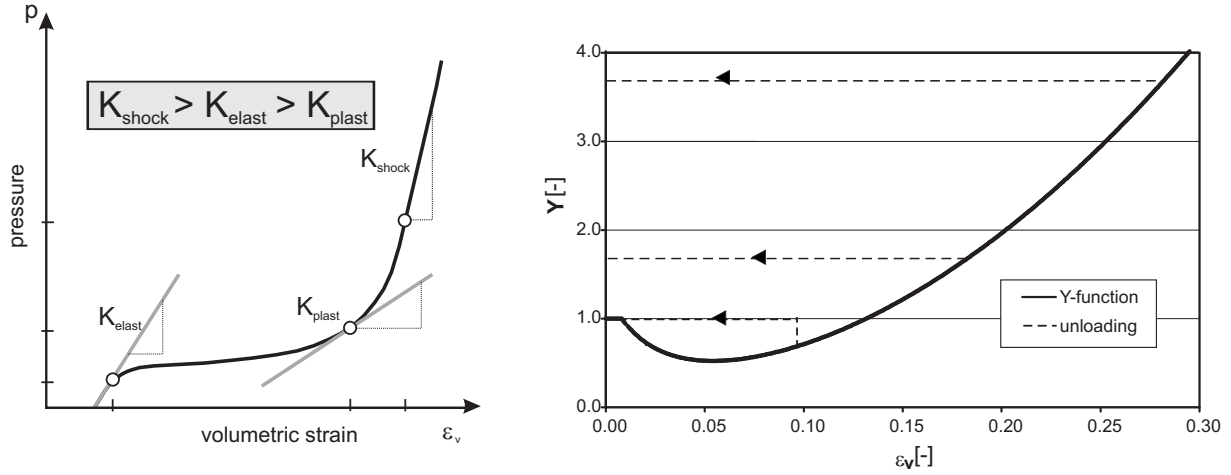


Figure 9: Hugoniot-curve – Y-function

The shape of the Y-function is shown by Schmidt-Hurtienne [10]

$$Y = \begin{cases} \left[ 1 - a_v \cdot \left( 1 - e^{-\frac{|\epsilon_v| - e_{v,th}}{e_v}} \right) \right] \cdot \left[ 1 + \left( \frac{|\epsilon_v| - e_{v,th}}{b_v \cdot e_v} \right)^2 \right] & \text{for } \epsilon_v < -e_{v,th} \\ 1 & \text{for } \epsilon_v \geq -e_{v,th} \end{cases} \quad (25)$$

The following parameters are used

$$\begin{aligned} e_{v,th} &= 0.008 \\ e_v &= 0.02 \\ a_v &= 0.7 \\ b_v &= 3.5 \end{aligned} \quad (26)$$

The Y-function for unloading is set to

$$Y_{unloading} = \begin{cases} 1 & \text{for } \max Y_{loading} = 1 \\ \max Y_{loading} & \text{for } \max Y_{loading} > 1 \end{cases} \quad (27)$$

### 3.3 Strain rate effect

The tensile and the compression strength increase with increasing strain rates. This has been shown in multiple experiments for example by Bischoff [4]. If concrete is blasted the strain rate reaches values of  $10^6 \text{ sec}^{-1}$ . It is not possible to get experimental results from concrete strength for strain rates higher than  $100 \text{ sec}^{-1}$ . So the strength factor for strain rates beyond this point is hypothetical. In contrary to the CEB Bulletin [5] the strength factor should be limited.

## 4 RESULTS

### 4.1 Three point bending test – static

The presented method is used to compute a concrete beam notched at the bottom side. The beam had no reinforcement and was tested by Körmeling [7]. The following material parameter

were used: Young's modulus  $E = 20\,000\text{ N/mm}^2$ , Poisson's ratio  $\nu = 0.20$ , tensile strength  $f_{t,static} = 2.4\text{ N/mm}^2$  and fracture energy  $G_f = 113\text{ N/m}$ . The dimensions of the specimen are shown in Figure 10.

The direction of the principle strains in the middle of the beam is very sensitive due to the low shear strain in this part. So the direction of the development of the crack is limited to the y-direction.

The calculated displacements of the beam are also shown in Figure 10. The calculation of the pre-peak displacements is in the range of the experiments. The displacements following the peak show that the reaction forces result by using the exponential fracture process zone are higher than the forces result by using the bilinear fracture process zone due to the lower crack closing stress by a small crack opening (Figure 8). The results with the bilinear fracture process zone show satisfactory deviations. In comparison to other authors like Rots [9] the deviations are in the same magnitude.

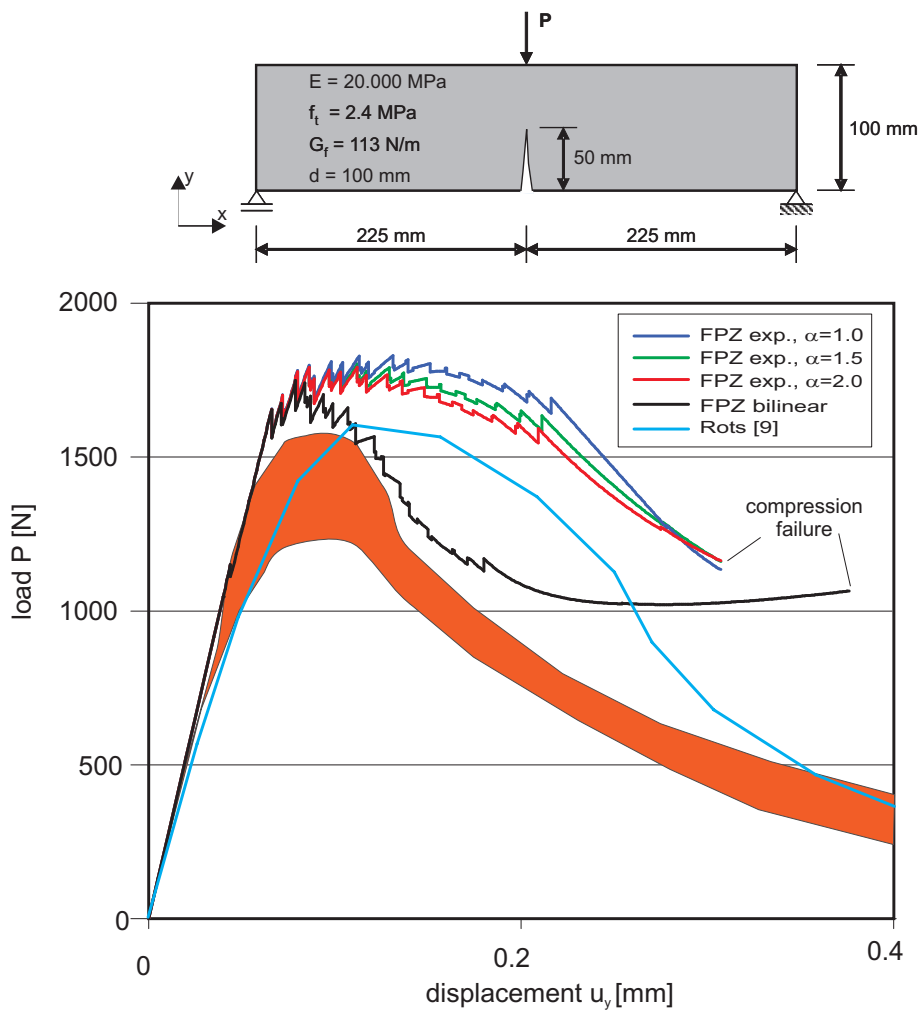


Figure 10: Three point bending test – comparison of experiments [7] with numerical results, exponential and bilinear FPZ

## 4.2 Development of shock waves

The proposed material model is implemented in an explicit time integration code. In order to test the Y-function (without the unloading part) a beam is loaded by a triangle load. Figure 11 shows that the wave following this loading is steepening due to the Y-function.

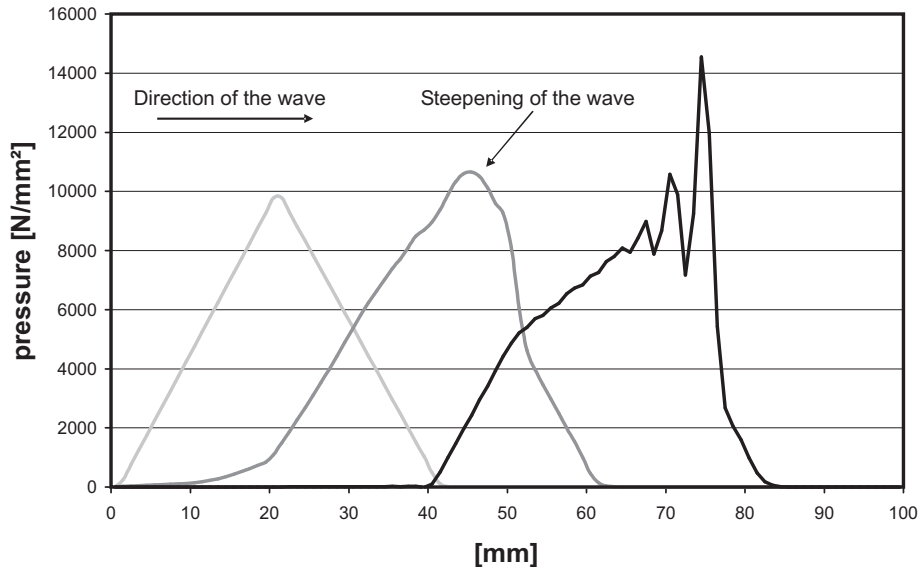


Figure 11: Development of the shock wave

## 4.3 Blasting of concrete

A contact detonation loads concrete with shock waves. At the Institute of Reinforced Concrete Structures and Building Materials at the University of Karlsruhe concrete slabs are loaded by an explosive to obtain the material parameters of high dynamic loaded concrete. The blasting results in a crater beneath the explosive. The concrete underneath the crater is highly compacted. Below this compacted range the concrete is damaged by cracks (Figure 12 – right).

The simulations of the experiments use the following parts of the material constitution:

- EFG and discrete cracks
- Limitation of distance between two cracks
- Limitation of the variation of the direction (necessary for EFG) – limitation of the crack radius
- Limitation of the crack velocity – Experiments from Curbach [6] show a limitation of the crack velocity to a value of 500 m/sec. Within the calculation the crack velocity is limited to this value.
- Y-function with unloading function
- Strain rate effect
- An easy contact algorithm

The result shows that the amplitude of the wave decreases very fast. The comparison of the cracks in the concrete shows that the parameters of the crack development have to be determined in order to get more sophisticated results (Figure 12 – left).

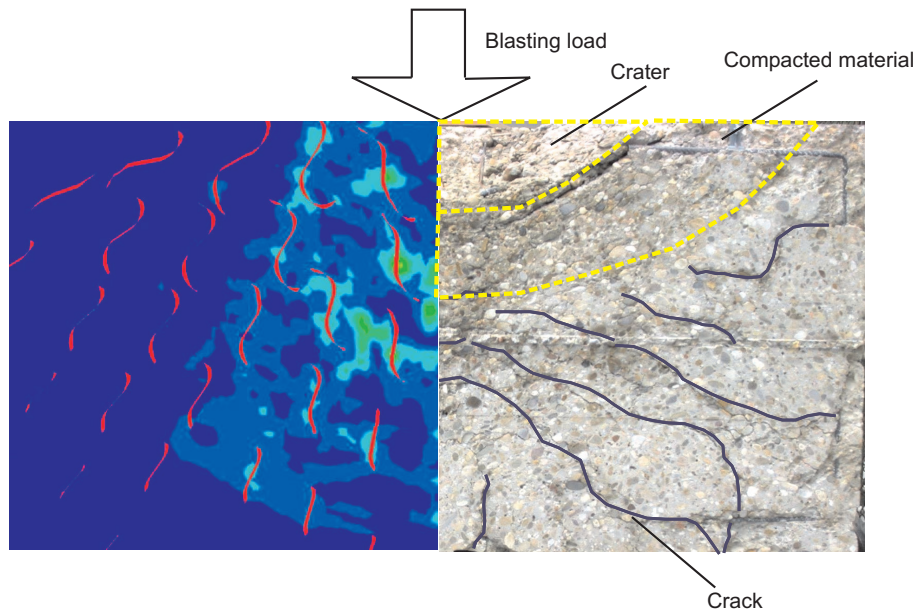


Figure 12: Cracks formation due to blast loading of concrete

## 5 CONCLUSIONS AND OUTLOOK

The element-free Galerkin method is a possibility to model discrete cracks in concrete. In combination with a fracture process zone it is possible to describe concrete under tension loading. The results of simulations of blasting show a good correlation with experimental data. The cracks resulting from the transverse tensile strain need a better adapted failure surface and smaller spaces between the cracks. This is to determine in further developments.

## REFERENCES

- [1] Jan Akkermann. *Rotationsverhalten von Stahlbeton-Rahmenecken*. Schriftenreihe des Instituts für Massivbau und Baustofftechnologie; Dissertation, Universität Karlsruhe, 2000.
- [2] Stephen Beissel and Ted Belytschko. Nodal Integration of the element-free Galerkin method. *Computer Methods in Applied Mechanics and Engineering*, 139:49–74, 1996.
- [3] T. Belytschko, Y.Y. Lu, and L. Gu. Element-free galerkin methods. *International Journal for Numerical Methods in Engineering*, 37:229–256, 1994.
- [4] P.H. Bischoff and S.H. Perry. Compressive behavior of concrete at high strain rates. *Materials and Structures*, 24:425–450, 1991.
- [5] CEB. Concrete Structures under Impact and Impulsive Loading - Synthesis Report 187. CEB Bulletins, 1988.

- [6] Manfred Curbach. *Festigkeitssteigerung von Beton bei hohen Belastungsgeschwindigkeiten*. Schriftenreihe des Instituts für Massivbau und Baustofftechnologie; Dissertation, Karlsruhe, 1987.
- [7] H.A. Koermeling and H.W. Reinhardt. Determination of the fracture energy of normal concrete and epoxy modified concrete. Technical Report No. 5-83-18, Stevin Laboratory, Delft University of Technology, 1983.
- [8] P.E. Roelfstra and F.H. Wittmann. *Fracture Toughness and Fracture Energy of Concrete*, chapter Numerical Method to Link Strain softening with Failure of Concrete, pages 163–175. Elsevier, 1986.
- [9] J.G. Rots. *Computational Modeling of Concrete Fracture*. PhD thesis, TH Delft, 1988.
- [10] Björn Schmidt-Hurtienne. *Ein dreiaxiales Schädigungsmodell für Beton unter Einschluss des Dehnrateneffekts bei Hochgeschwindigkeitsbelastung*. Schriftenreihe des Instituts für Massivbau und Baustofftechnologie; Dissertation, Universität Karlsruhe, 2001.
- [11] Stepan P. Timoschenko and James N. Goodier. *Theory of elasticity*. McGraw-Hill, 1970.
- [12] G. Ventura, J.X. Xu, and T. Belytschko. A vector level set method and new discontinuity approximations for crack growth by EFG. *International Journal for Numerical Methods in Engineering*, 54(6):923–944, 2002.